Journal of Power Sources 188 (2009) 468–474

Contents lists available at ScienceDirect

Journal of Power Sources

journal homepage: www.elsevier.com/locate/jpowsour

High-resolution in-plane investigation of the water evolution and transport in PEM fuel cells

Christoph Hartnig[a,*], Ingo Manke[b,c], Robert Kuhn[a], Sebastian Kleinau[a], Jürgen Goebbels[d], John Banhart[b,c]

[a] Centre for Solar Energy and Hydrogen Research Baden-Württemberg, Helmholtzstraße 8, 89081 Ulm, Germany
[b] Institute of Materials Science and Technology, Berlin Institute of Technology, Hardenbergstr. 36, 10623 Berlin, Germany
[c] Helmholtz-Institute for Materials and Energy, Glienicker Str. 100, 14109 Berlin, Germany
[d] Bundesanstalt für Materialforschung und -prüfung (BAM), Unter den Eichen 87, 12205 Berlin, Germany

ARTICLE INFO

Article history:
Received 20 September 2008
Received in revised form 31 October 2008
Accepted 8 December 2008
Available online 13 December 2008

Keywords:
Water management
In situ detection
Gas diffusion layer
Synchrotron radiography

ABSTRACT

High-resolution synchrotron X-ray radiography is used to study the evolution of primary water clusters and the transport of liquid water from the catalyst layer through the gas diffusion layer (GDL) to the gas channels of a low temperature polymer electrolyte membrane (PEM) fuel cell. The liquid water content is quantified separately in the respective components; in the hydrophobic microporous layer (MPL) almost no liquid water can be observed. In the adjacent GDL, depending on the current density i_0 water clusters are formed which lead to a diffusion barrier for the reactant gases. Water transport dynamics are explained and a recently proposed eruptive mechanism describing the transport from the GDL to the gas channels is imaged in a pseudo three-dimensional representation [A. Bazylak, D. Sinton, Z.-S. Liu, N. Djilali, J. Power Sources 163 (2007) 784–792; S. Litster, D. Sinton, N. Djilali, J. Power Sources 154 (2006) 95–105; I. Manke, Ch. Hartnig, M. Grünerbel, W. Lehnert, N. Kardjilov, A. Haibel, A. Hilger, H. Riesemeier, J. Banhart, Appl. Phys. Lett. 90 (2007) 174105]. Based on a high temporal resolution the dynamics of the liquid water transport are observed; transient conditions resembling dynamic operation of the fuel cell are studied and an estimation of the time required to reach equilibrium conditions is given. The obtained spatial resolution of 3 μm is far below commonly used techniques such as neutron radiography or ^{1}H NMR. Fundamental aspects of cluster formation in hydrophobic/hydrophilic porous materials as well as processes of multi-phase flow are addressed.

© 2008 Elsevier B.V. All rights reserved.

1. Introduction

In polymer electrolyte fuel cells (PEMFCs) the chemical energy stored in hydrogen and oxygen is converted to electrical and thermal power [4–6]; if the hydrogen is produced based on regenerative energy sources such as wind or solar energy, almost no carbon dioxide will evolve which is, in the course of the current discussions and environmental considerations, a highly desirable situation. A variety of factors influence the broad market introduction, the most striking ones are besides the price of the fuel cells (which is considerably high due to the noble metal content) the long-term stability and an optimum performance over a broad range of operating conditions.

In Fig. 1 the setup of a state-of-the-art PEM fuel cell is displayed which is employed to convert the electrochemically stored energy of hydrogen and oxygen to water. Water plays a crucial role in the fuel cell processes: in the electrochemical reaction, water is involved in elementary reaction steps of oxygen reduction; the presence of water is also required to enable the desorption of the oxidation products from the surface to migrate to the membrane. For the polymer electrolyte membrane (PEM), certain humidity is necessary to keep the protonic conductivity [7–9]. A dry membrane undergoes structural changes and the conductivity collapses [10,11]. In the adjacent gas diffusion layer (GDL), water is usually transported in gas phase from the catalyst layer to the gas channels of the flow field. However, at high current densities (or in other words, at high water production rates) the saturation pressure of water can be exceeded leading to the existence of two phases, water vapor and liquid water. The latter phase might lead to blocked pathways in the GDL and the catalyst layers which in turn limits the maximum achievable power density. These two-phase or even multi-phase flow phenomena are not limited to fuel cell processes but play an important role in several natural and technical processes: water transport through pores in rocks and sands takes place whenever stony materials are in contact with a humid atmosphere [12]. Immiscible phases also appear in combinations of hydrophobic

* Corresponding author. Tel.: +49 731 9530 612; fax: +49 731 9530 666.
E-mail address: christoph.hartnig@zsw-bw.de (C. Hartnig).

0378-7753/$ – see front matter © 2008 Elsevier B.V. All rights reserved.
doi:10.1016/j.jpowsour.2008.12.023

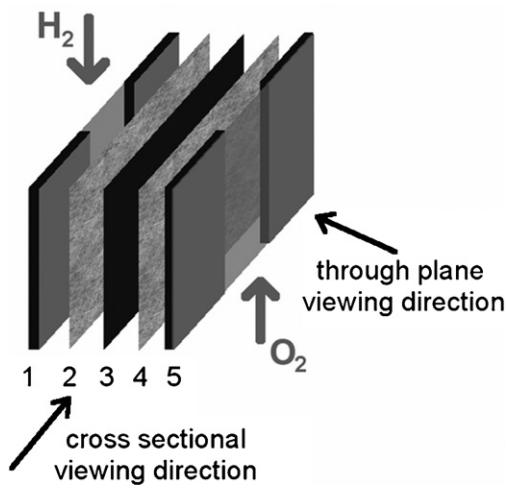

Fig. 1. Fuel cell setup and viewing directions: 1 and 5 are the anodic resp. cathodic flow field, 2 and 4 the gas diffusion layers (GDL) and 3 is the membrane-electrode-assembly (MEA). The cross-sectional (in plane) view allows for an investigation of the water transport from the catalyst layer to the gas channel.

and hydrophilic materials which are present in various engineering applications, e.g., in petroleum engineering. The exploration of crude oil from oil sands by means of hot water and steam is a typical process which can be described as a multi-phase system with the water forming a contact layer on the largely hydrophilic sand surface [12]. These processes have been described by numerous theoretical models [13], most of them without experimental verification.

Several approaches employing modified fuel cells with transparent parts were proposed to visualize the water transport [14–16]. However, such modifications lead to unpredictable interference with the water distribution. ^{1}H NMR suffers thereby from the existence of metallic parts such as end plates [17–19]. Due to the high sensitivity to hydrogen, neutron radiographic visualization became important to detect liquid water in operating fuel cells [20–33]. Most of these works focus on the transport of rather large droplets and accumulation of water in the flow field channels and the GDL taking the top view on the electrochemically active area (through plane) into account (compare to Fig. 1). Recently, several groups investigated the in-plane water distribution by means of neutron radiography [20,22,24–31,33]; depending on the detector system spatial resolutions even below 30 μm have been obtained [30,31]. However, the severely enhanced spatial resolution is counterbalanced by long image-to-image times in the range of several minutes. These limitations were overcome by means of synchrotron X-ray radiography. The initial formation of small water agglomerations, the transport processes in the GDL and the transition from the GDL to the gas channel are visualized engaging a resolution down to 3 μm [3]. Depending on the operating conditions such as the rate of current production, the condensation of water vapor forming liquid water in the GDL has been observed. The influence of the degree of hydrophobicity of the different components such as microporous layer (MPL) and GDL on the existence of liquid water can be tracked. The results allow for an in-depth analysis and understanding of factors influencing the water management which resembles a key issue for a high performance and a long-term stability of fuel cells. As obvious from the presented results, not only the effects of different surface properties in terms of hydrophobicity can be taken into account, but fundamental transport mechanisms known from theoretical models which are usually applied to describe transport processes in porous environments have been visualized as well; caused by the surface tension of water in a hydrophobic surrounding, a so-called compact cluster growth initiates the formation of larger clusters which erupt from the porous media in a consecutive combination of Haines jumps and choke-off effects.

2. Experimental

A single channel fuel cell setup has been designed to fulfill two preconditions, the resemblance to a realistic system as well as the possibility to render the different components of the fuel cell and to gain a cross-sectional insight into the evolution and transport of water. A serpentine flow field design was used with an electrochemically active area of 12 cm^2 machined in graphite composite material. SGL Sigracet 10 BB gas diffusion material with a poly-tetrafluorethylene (PTFE) loading of 5% was applied to both electrodes, and a GORE 5621 MEA with a membrane thickness of 40 μm was used with catalyst loadings of 0.3 mg cm^{-2} at the anode and 0.4 mg cm^{-2} at the cathode [34]. The cell is kept tight by silicon gaskets. The upright positioned fuel cell was operated at standard parameter settings at all performed tests; the cathodic utilization rate u_C describing the fraction of gas (air) consumed along the reactive area is set to u_C = 25%, the anodic utilization rate to u_A = 90%, and the temperature of the stack to T = 60 °C. The cathodic gas stream was humidified at a dew point of 25 °C, while the anodic gas stream remained unhumidified. Ambient pressure was kept at the media outlets. The current density i_0 which determines the amount of water produced in the electrochemical reaction is varied between 300 and 700 mA cm^{-2}. Each operation point has been set for 20 min so that equilibrated conditions were reached when monitoring the liquid water content as function of current density. For the observation of the transient behavior of the water content, the switch of the current density has been undertaken during imaging. The humidification of the gas flow is below complete saturation at the chosen operating parameters, i.e., formed water droplets can evaporate and are not only shoved away by the gas flow.

The synchrotron X-ray energy was chosen in a way to strongly enhance the sensitivity to water; the contrast between the attenuation of water and fuel cell components such as the surrounding gas diffusion material and gaskets is thereby optimized. The experiments were performed at the tomography facility of the BAMline at the synchrotron BESSY (Berlin, Germany). A monochromatic X-ray beam with an energy of 13 keV and an energy resolution of about $\Delta E/E = 10^{-2}$ was applied. A Princeton (VersArray 2048B) CCD camera with 2048 pixel × 2048 pixel was used to capture images up to 7 mm × 7 mm large with corresponding image pixel sizes between 1.5 and 3.5 μm which correspond to a physical spatial resolution of 3–7 μm. The measurement time per image was between 3–5 s, 1 s for exposure and about 2–4 s for data read-out.

3. Results

3.1. Dependence of water content on current density

In Fig. 2 a cross-sectional view of a fuel cell is displayed in which the individual components of a cell can be clearly differentiated. Images taken during the measurements are normalized with respect to a water free (dry) cell. Thereby, the unhumidified reactant gas flow is switched on and no electric load is applied so that no net water is produced (the so-called open-circuit voltage can be observed which is due to the electrochemical potential formed at the electrodes). Fig. 2 is derived from the normalization where components such as gaskets are subtracted (quotient *wet image*/*dry image*) and do not influence the results; water can hereby be identified as bright spots. At the bottom, a schematic drawing of the cell components is added clarifying the different parts of the image: the core of the fuel cell, the membrane-electrode-assembly (MEA) consisting of the perfluorinated sulfonic acid (PFSA) membrane with

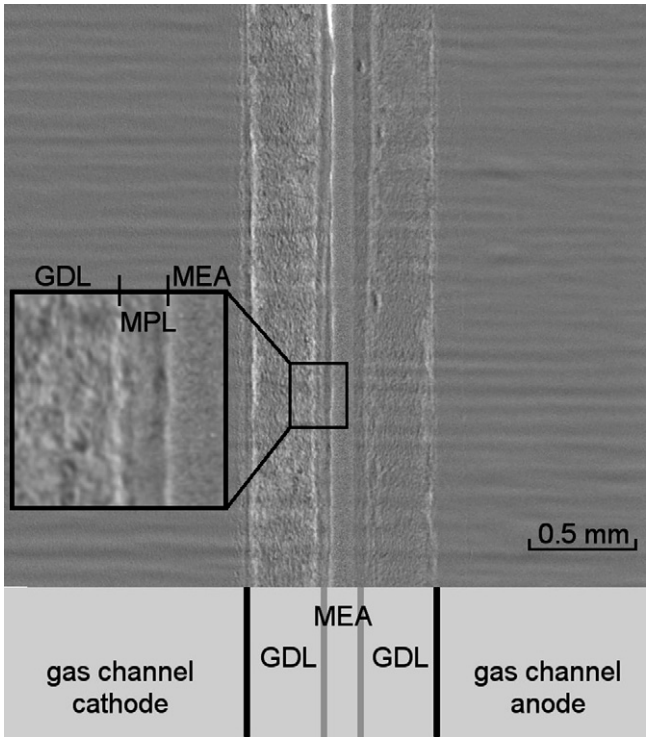

Fig. 2. Normalized image of the cross-section of a PEM fuel cell. The image has been normalized with respect to an empty (water free) cell. Water agglomerates can be identified in this representation as bright spots; the schematic drawing of the cell in the lower part clarifies the respective components. The differentiation between MPL and GDL is demonstrated in the inset.

the catalyst attached on both sides in the centre of the cell exhibits a high absorption coefficient. Since the energy of the X-ray beam has been chosen to achieve a maximum sensitivity towards water, the platinum content of the supported catalyst leads to the aforementioned high absorption coefficient. The count rate of the incident beam is thereby less than a few percent compared to neighboring parts. Although some slight blurring caused by small angle scattering might exist, its overall contribution is negligible compared to the effect due to refraction, i.e., phase contrast effects that yield a sharp signal variation at edges.

The central part of the cross-section is magnified in the inset of Fig. 2. At both sides of the MEA are the GDLs. Attached on the GDL next to the MEA is a so-called MPL which can be distinguished from the carbon fiber as a fine grained structure. The MPL mainly consists of carbon black and PTFE which results in a predominantly hydrophobic material. The MPL ensures an equilibrated water content of the catalytic area; due to its microstructure with very hydrophobic and therefore water-free spots caused by the PTFE, the MPL allows for the diffusion of reactant gases to the catalyst layer. To both sides of the GDLs the cathodic, respectively anodic flow field channels and the back wall of the flow field can be identified.

In an operating fuel cell, water is predominantly formed at the cathode; in addition, water molecules are transported from the anode through the membrane to the cathode by the electro-osmotic drag leading to high water concentrations on the cathode and, in the worst case, to drying phenomena on the anode. However, the gradient of the water concentration invokes the back-diffusion where the water is transported in the opposite direction from the cathode to the anode which ensures a sufficient humidification of the anode. Depending on the current density one of the processes is favored above the other which will be addressed in more detail below.

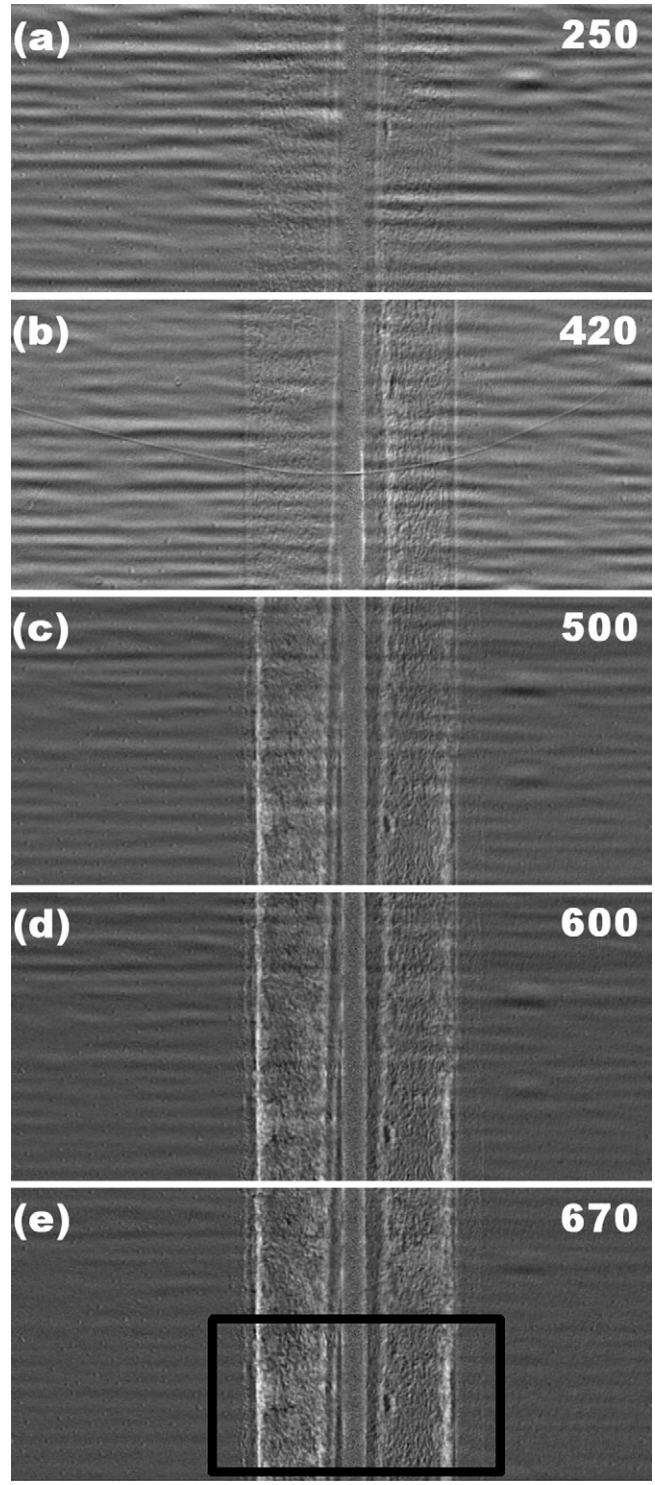

Fig. 3. Liquid water formation as function of current density i_0: (a)–(e), (a) at $i_0 = 250\,\mathrm{mA\,cm^{-2}}$ hardly any liquid water is formed; (b): larger values of i_0 ($420\,\mathrm{mA\,cm^{-2}}$) lead to initial water clusters on the cathode (white spots); at $i_0 = 500\,\mathrm{mA\,cm^{-2}}$ water clusters appear at the anode; (c)–(e): from $i_0 = 500\,\mathrm{mA\,cm^{-2}}$ onwards water clusters are present to a large extent in both gas diffusion electrodes. Horizontal stripes are artifacts caused by thermal fluctuation of the monochromator setup; the black box depicts the area used to quantify the water content as displayed in Fig. 5.

Normalized images of the fuel cell operating at different current densities are displayed in Fig. 3. The current density i_0 determines the rate of water production; increasing i_0 leads to enhanced water formation and vice versa. At low current den-

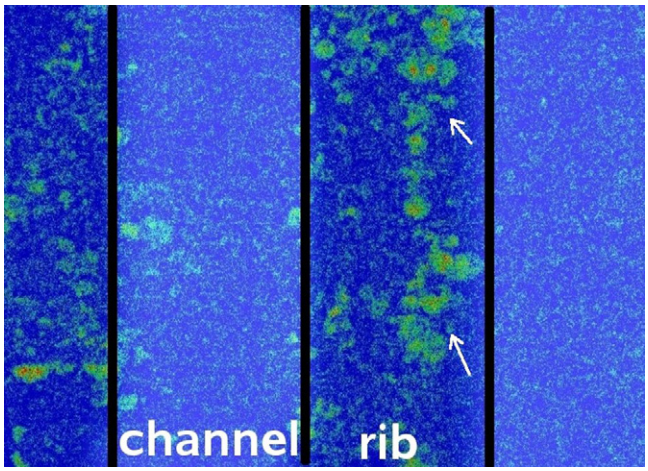

Fig. 4. Through-plane observations show clearly the initial spots of liquid water formation (bright spots) beneath the ribs of the flow field channel.

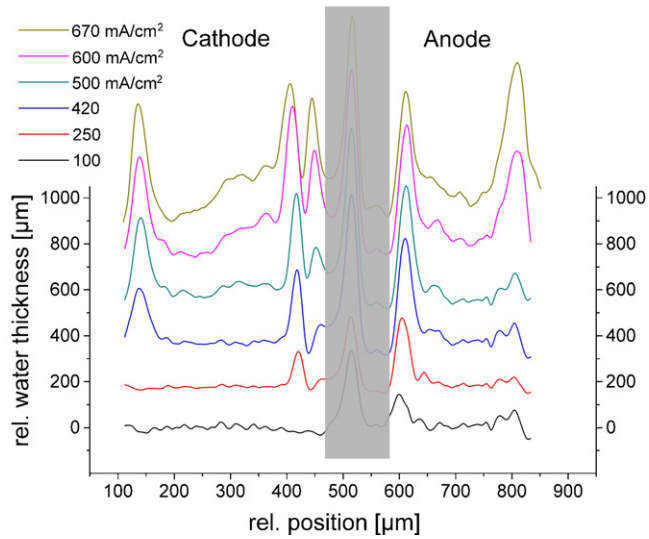

Fig. 5. Quantification and location of liquid water in the cathodic (C) and anodic (A) gas diffusion layer. Depending on the operating conditions, one or two diffusion barriers formed by liquid water can be detected. The water content of the MEA is shaded due to the low statistics caused by high absorption coefficients of platinum.

sities (i_0 = 250 mA cm^{-2}, Fig. 3a) hardly any liquid water can be detected; product water from the electrochemical reaction is transported mainly in gas phase, phenomena like two-phase flow do not play a significant role at these operating conditions. With increasing current density (i_0 = 420 mA cm^{-2}, Fig. 3b) liquid water appears primarily in the cathodic GDL which is the place where the protons transported through the membrane recombine with the reaction products of the oxygen reduction reaction to form liquid water. At higher current densities at both the anodic and cathodic side liquid water is observed (i_0 > 500 mA cm^{-2}, Fig. 3c–e) resulting from the back diffusion due water gradient between anode and cathode. Two main positions of liquid water agglomerations can be estimated along the cross-section. The first one located close to the gas channel and the second one next to the MPL. Due to its hydrophobic nature, the MPL contains hardly any liquid water. In both cases the liquid water is located in the area beneath the ribs of the flow field forming a diffusion barrier for the reactant gases. The formation of this diffusion barrier can be explained by slight temperature differences between the electrochemically active area and the adjacent GDL and the MPL: liquid water, which might exist at the catalyst surface, evaporates and diffuses through the MPL where due to the high hydrophobicity no condensation can take place. Once the water vapor reaches the GDL, the gas pressure of the water is reached and condensation on hydrophilic spots steps in next to the MPL. The further transport of these agglomerates can either take place in gas phase or in liquid phase and is subject of ongoing research activities. The exact position and a differentiation between spots beneath the ribs or the lands of the flow field can be determined by means of a perpendicular view (through plane) rendering the clustering beneath the ribs obvious (Fig. 4, compare to Fig. 1 for viewing directions). In the areas under the channel of the flow field hardly any water clusters can be detected in the gas diffusion media underlining the liquid water-free conditions. Under the ribs of the flow field water clusters are visible and marked by arrows in Fig. 4; due to several interacting factors liquid water preferably evolves under the lands of the flow field: not only is the porosity of the GDL reduced due to the compression but also the electrical conductivity is increased. The previously employed explanation of elongated diffusion pathways compared to areas with a direct connection to the gas channel cannot be applied based on the location next to the land of the flow field (a detailed explanation of the evolution and position of the water clusters is given in Ref. [3]).

Liquid water agglomerates were quantified by summation of 100 rows along the marked area in Fig. 3. The relative amounts along the cross-section as a function of i_0 are displayed in Fig. 5. The local water thickness is calculated in a standardized way based on the attenuation coefficient of liquid water at the corresponding energy; more details can be found in Ref. [3]. As already estimated qualitatively from Fig. 3, at low current densities only small amounts of water condense in the vicinity of the MPL indicating an almost liquid water free situation. At higher current densities larger clusters are formed which might act as diffusion barrier for reactant gases. A first maximum of the liquid water distribution is located directly in the GDL in close proximity to the MPL; a second maximum resides beneath the rib next to the channel. Water stemming from the electrochemical reaction condenses near the catalyst, caused by slightly decreased temperatures (compared to the catalytically active spots) and mass transport limitations due to the external humidification. On the anode, a similar behavior can be observed: contrary to the processes on the cathode, already at low current densities (i_0 = 300–400 mA cm^{-2}) primary spots of liquid water accumulate in the GDL close to the MPL. With increasing values of i_0 the amount of liquid water increases and a more or less dense layer is formed. A second diffusion barrier close to the channel of the flow field caused by liquid water as observed at the cathode is not observed at the anode where no transport limitations due to the humidification exist. Only at higher current densities (i_0 > 500 mA cm^{-2}) a significant second peak is observed which is comparable to the one formed on the cathode. The maxima of the liquid water content close to the reaction layer appear higher at the anode for all but the highest investigated current density. The aforementioned balance between the back diffusion and the electro-osmotic drag is hinted at by this distribution: only at high current densities the back diffusion is outweighed by the electro-osmotic drag. Therefore, the operation mode implying an external humidification of just the cathode to humidify the anode has been proven on a microscopic scale.

3.2. Transient conditions

The major advantage of synchrotron based methods compared to many other in situ imaging methods are the aforementioned short image-to-image times which allow for a detailed investigation of fast processes and, as demonstrated here, the observation of transient conditions. The response of the water content at

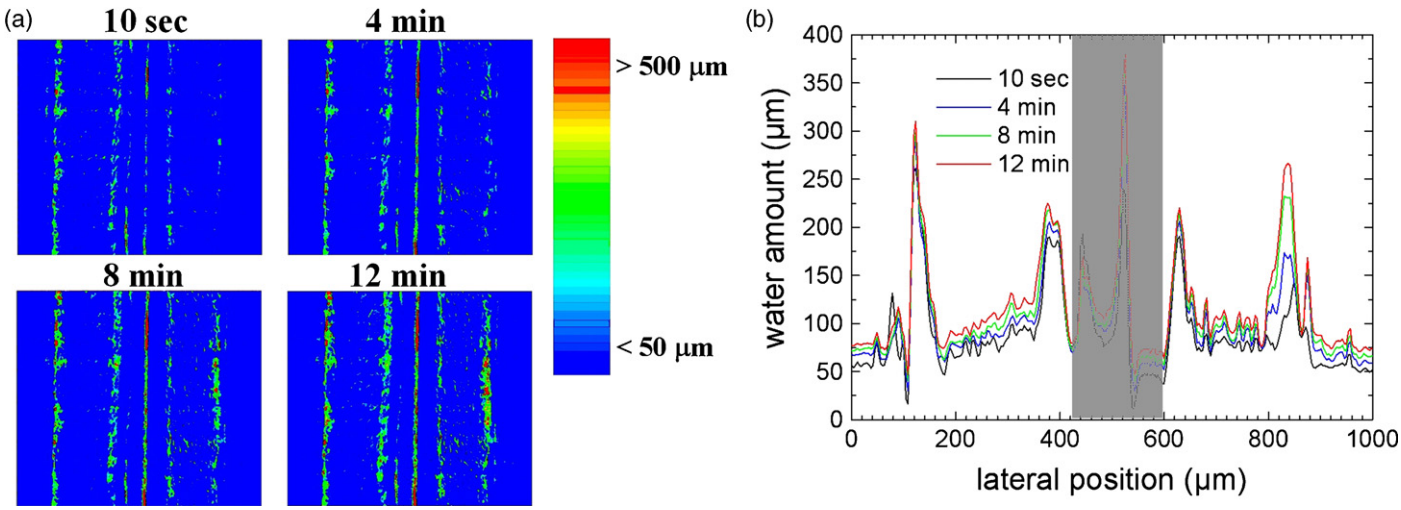

Fig. 6. Dynamics of water formation in the gas diffusion layer at transient current densities: (a) visualization of the water distribution and (b) quantification of the water amount in the different layers. The jump in the current density from $i_0 = 500$ to $i_0 = 600\,\mathrm{mA\,cm^{-2}}$ is followed by an increase of the liquid water content in the anodic gas diffusion layer; the degree of filling on the cathode already reached a stationary point where only slight changes in the anodic water content can be observed.

transient currents is described in more detail in Fig. 6. Transient currents describe a situation of changing power requests: in contrast to stationary conditions where none of the operating conditions are changed, in the transient regime, e.g., the current density is switched from one value to the next one resembling a dynamic operation mode as, e.g., in automotive applications. At $t = 0$ the current density is switched from $i_0 = 500$ to $i_0 = 600\,\mathrm{mA\,cm^{-2}}$. Based on the findings in Fig. 5, this jump of the current density has been chosen in order to follow the increase of cathodic water content and the formation of the peak next to the channel on the anode. Qualitatively, an increase of the water content especially in the anodic GDL can be estimated from Fig. 6a. After approximately 10–15 min, an equilibrium condition is reached on both electrodes where the water content is constant. A quantification of the time dependence of the liquid water content is displayed in Fig. 6b: on the cathode, the two maxima next to the MPL and beneath the rib of the flow field quickly reach the maximum due to the increased water production and the contribution from the adjusted humidified gas stream. Once the water content has reached a stationary condition, additional water is transported to the gas channel with only a slight increase of the total amount in the GDL. On the anode, the maximum of the water distribution adjacent to the MPL does not change significantly with increasing water production rate. A second maximum develops next to the gas channel which is comparable to the distribution on the cathode and might influence the gas transport by building a diffusion barrier. Due to the much slower transport of water through the membrane compared to gas phase as on the cathode, the equilibrium is reached after a much longer period. This water thickness has not been observed until a certain threshold value of the current density is reached which is (at the chosen operating conditions) between 500 and $600\,\mathrm{mA\,cm^{-2}}$.

3.3. Dynamics

Besides the mere location of the agglomerates the dynamics of the liquid water transport from the catalytic layer to the flow field channel is of major interest not only to shed light on the transport processes but to compare the mechanisms found to theoretical descriptions and to estimate the contribution of multi-phase flow phenomena to the overall transport. The transport of liquid water is elucidated in more detail in Fig. 7. Displayed are two consecutive images with a time resolution of 5 s and the differential image (technically spoken, the quotient image of the two images) at a current density at which liquid water is observed ($i_0 = 500\,\mathrm{mA\,cm^{-2}}$). The two water layers close to the channel and next to the MPL at the right side have already been described. Due to the integral nature of these images (two areas beneath the ribs to each side of the channel are considered) a distinction cannot be made in terms of water in the foreground and in the rear part. Within the observation period between two images a water droplet is formed in the channel; small water clusters incorporated in the prevalently hydrophobic GDL merge to form larger ones which finally erupt ('burst') from the GDL to the gas transport channels.

A different way to interpret the observed phenomena is based on a description as employed in geological disciplines: compact cluster growth of a non-wetting liquid (water) in hydrophobic pores results from Haines jumps which are caused by interfacial advances in a very much localized section. The capillary pressure in the neighboring entity is lower than in the vicinity which causes the smaller clusters to burst to neighboring pores. The transition (avalanche) to the gas channel is triggered by the same factors, whereas for this process an additional mechanism can be observed. The bursting droplet carries away water from the GDL and the 'supply' is not sufficient to fill the pores. These choke-offs lead to empty pores which are filled afterwards and the cycle starts again [35–37]. The eruptive mode has been proposed on the basis of previous neutron radiographic experiments [38] and was verified in recent ex situ and in situ experiments [1–3]. The differential plot of two images (Fig. 7c) allows for a determination of the origin and the new position of the liquid water and gives an approximation of the catchment area for droplet formation which might cover more than $1\,\mathrm{mm^2}$.

The cyclic behavior of the transport process is quantified by means of the amount of liquid water in the gas channel (Fig. 8) where the peaks denote erupted water droplets. Within the whole transport process, the bursts are observed at the same position indicating the existence of preferred pathways in the porous material. In recent ex situ investigations, bursting water droplets have been observed and the formation of preferred apertures on the GDL surface has attributed to broken fibers in the porous material. The sites of fractures caused by the material compression at the edges of the flow field ribs lead to hydrophilic spots in a hydrophobic surrounding at which the water might preferably condense [2]. As the eruptive mechanism takes place only at current densities $i_0 > 400\,\mathrm{mA\,cm^{-2}}$, a current threshold can be estimated above which the contribution of liquid water might raise the need for micro-

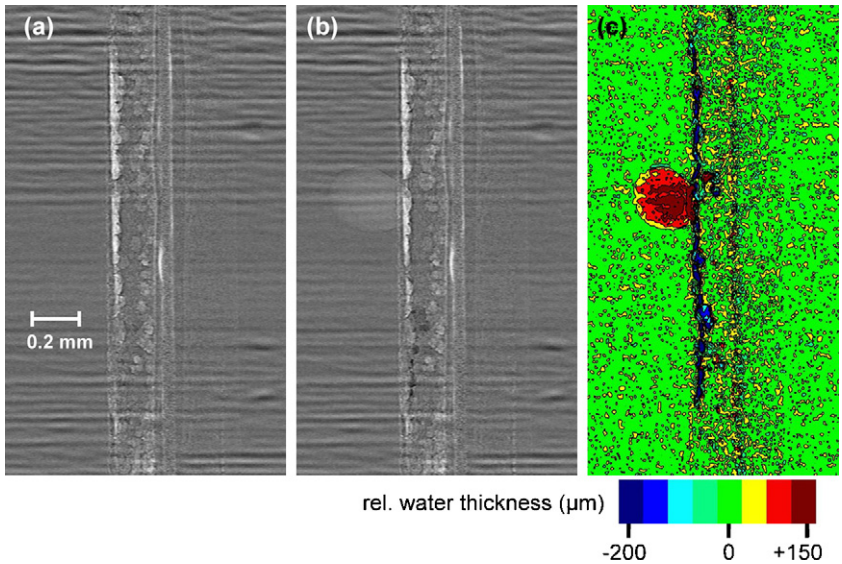

Fig. 7. Eruptive water transport from the gas diffusion media to the flow field channel: (a) and (b) white spots denote water agglomerates before and after water eruption; (c) differential image of the images (a) and (b); blue: water clusters which were transported to the channel to form the droplet (red). The interplay of the preferably hydrophobic substrate and the water results in an eruptive behavior of the transport process (detailed operating conditions are given in the text).

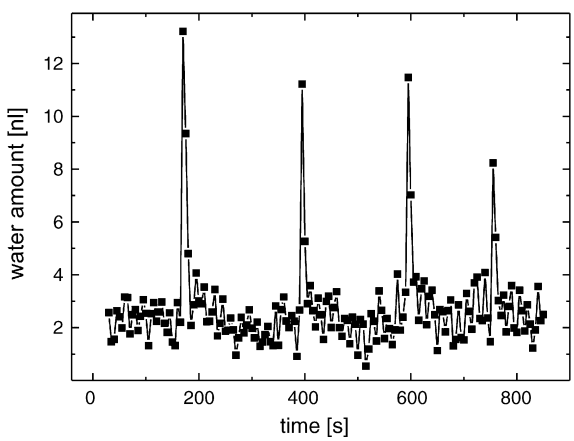

Fig. 8. Cyclic water eruptions. The cyclic character of the eruptive water transport mechanism is determined by the amount of liquid water in the channel (detailed operating conditions are given in the text).

scopic non-continuum models to adequately describe the water transport [39–44,47].

4. Conclusion

We have investigated the cross-sectional transport of liquid water in porous gas diffusion materials as employed in low temperature fuel cells by means of synchrotron X-ray radiography with a spatial resolution of 3 μm and a time resolution of 5 s. The water distribution in the GDL strongly depends on the water production rate (the current density) and up to two different diffusion barriers caused by liquid water were detected at high current densities. The position of these diffusion barriers depends on the hydrophobic/hydrophilic properties of the employed materials.

Transient conditions caused by changes of the current density have been observed with regard on acquiring equilibrium conditions in the water distribution; a delay of up to 12 min is needed to achieve a static condition at current densities exceeding 500 mA cm^{-2}.

The microscopic transport of liquid water is described by consecutive Haines jumps leading to a compact water cluster growth in the GDL. At the transition from the GDL to the gas channel, choke-off effects cause emptied pores which are filled gradually and lead to a cyclic transport behavior. These results approve furthermore transport theories used within the framework of percolation theory [45,46].

The presented finding might serve as basis to develop tailor-made materials with customized properties to remove excess liquid water more efficiently. A uniform distribution of the liquid water might finally lead to an increased performance and durability. Modeling approaches of multi-phase flows can be adapted based on these results and estimations on the amount of liquid water involved in the overall two-phase water transport might be deduced [47,48].

Acknowledgements

We would like to thank Frank Häußler and Joachim Scholta for their support at constructing the fuel cell and fruitful discussions. The research activities were funded by the German Federal Ministry for Education and Science (BMBF) under grant numbers 03SF0324A and 03SF0324F (RuNPEM).

References

[1] A. Bazylak, D. Sinton, Z.-S. Liu, N. Djilali, J. Power Sources 163 (2007) 784–792.
[2] S. Litster, D. Sinton, N. Djilali, J. Power Sources 154 (2006) 95–105.
[3] I. Manke, Ch. Hartnig, M. Grünerbel, W. Lehnert, N. Kardjilov, A. Haibel, A. Hilger, H. Riesemeier, J. Banhart, Appl. Phys. Lett. 90 (2007) 174105.
[4] B. Steele, A. Heinzel, Nature 414 (2001) 345–352.
[5] F. Bruijn, Green Chem. 7 (2005) 132–150.
[6] L. Carrette, K.A. Friedrich, U. Stimming, Fuel Cells 1 (2001) 5–38.
[7] M. Eikerling, S.J. Paddison, L.R. Pratt, T.A. Zawodzinski, Chem. Phys. Lett. 368 (2003) 108–114.
[8] H.L. Yeager, A. Steck, J. Electrochem. Soc. 128 (1991 1880).
[9] K.-D. Kreuer, S.J. Paddison, E. Spohr, M. Schuster, Chem. Rev. 104 (2004) 4637.
[10] G. Gebel, Polymer 41 (2000) 5829–5838.
[11] P.W. Majsztrik, M.B. Satterfield, A.B. Bocarsly, J.B. Benziger, J. Membr. Sci. 301 (2007) 93–106.
[12] V. Mani, K.K. Mohanty, J. Pet. Sci. Eng. 23 (1999) 173–188.
[13] C.-Y. Wang, P. Cheng, Int. J. Heat Mass Transfer 39 (1996) 3607–3618.
[14] K. Tüber, D. Pócza, C. Hebling, J. Power Sources 124 (2003) 403–414.
[15] P. Argyropoulos, K. Scott, W.M. Taama, Electrochim. Acta 44 (1999) 3575–3584.
[16] D. Spernjak, A.K. Prasad, S.G. Advani, J. Power Sources 170 (2007) 334–344.
[17] K.W. Feindel, S.H. Bergens, R.E. Wasylishen, Phys. Chem. Chem. Phys. 9 (2007) 1850–1857.
[18] K.W. Feindel, S.H. Bergens, R.W. Wasylishen, J. Power Sources 173 (2007) 86–95.

[19] K.W. Feindel, S.H. Bergens, R.E. Wasylishen, J. Am. Chem. Soc. 128 (2006) 14192–14199.
[20] M.A. Hickner, N.P. Siegel, K.S. Chen, D.N. McBrayer, D.S. Hussey, D.L. Jacobson, M. Arif, J. Electrochem. Soc. 153 (2006) A902–A908.
[21] D.L. Ludlow, C.M. Calabrese, S.H. Yu, C.S. Dannehy, D.L. Jacobson, D.S. Hussey, M. Arif, M.K. Jensen, G.A. Eisman, J. Power Sources 162 (2006) 271–278.
[22] A. Turhan, K. Heller, J.S. Brenizer, M.M. Mench, J. Power Sources 160 (2006) 1195–1203.
[23] J.J. Kowal, A. Turhan, K. Heller, J. Brenizer, M.M. Mench, J. Electrochem. Soc. 153 (2006) A1971–A1978.
[24] D. Kramer, J. Zhang, R. Shimoi, E. Lehmann, A. Wokaun, K. Shinohara, G.G. Scherer, Electrochim. Acta 50 (2005) 2603–2614.
[25] J. Zhang, D. Kramer, R. Shimoi, Y. Ono, E. Lehmann, A. Wokaun, K. Shinohara, G.G. Scherer, Electrochim. Acta 51 (2006) 2715–2727.
[26] I.A. Schneider, D. Kramer, A. Wokaun, G.G. Scherer, Electrochem. Commun. 7 (2005) 1393–1397.
[27] Ch. Hartnig, I. Manke, N. Kardjilov, A. Hilger, M. Grünerbel, J. Kaczerowski, J. Banhart, W. Lehnert, J. Power Sources 176 (2008) 452–459.
[28] I. Manke, Ch. Hartnig, N. Kardjilov, M. Messerschmidt, A. Hilger, M. Strobl, W. Lehnert, J. Banhart, Appl. Phys. Lett. 92 (2008) 244101.
[29] I. Manke, Ch. Hartnig, M. Grünerbel, J. Kaczerowski, W. Lehnert, N. Kardjilov, A. Hilger, W. Treimer, M. Strobl, J. Banhart, Appl. Phys. Lett. 90 (2007) 184101.
[30] M.A. Hickner, N.P. Siegel, K.S. Chen, D.S. Hussey, D.L. Jacobson, M. Arif, J. Electrochem. Soc. 155 (2008) 427.
[31] P. Boillat, D. Kramer, B.C. Seyfang, G. Frei, E. Lehmann, G.G. Scherer, A. Wokaun, Y. Ichikawa, Y. Tasaki, K. Shinohara, Electrochem. Commun. 10 (2008) 546.
[32] R. Satija, D.L. Jacobson, M. Arif, S.A. Werner, J. Power Sources 129 (2004) 238–245.
[33] A.E. Geiger, Fuel Cells 2 (2002) 92–98.
[34] Certain trade names and products are mentioned in the text in order to specify the experimental setup and procedure. In no case does such an identification imply recommendation or endorsement nor does it imply that these materials are necessarily the best available for the application.
[35] B. Berkowitz, R.P. Ewing, Surv. Geophys. 19 (1998) 23–72.
[36] L. Paterson, A.P. Sheppard, M.A. Knackstedt, Phys. Rev. E 66 (2002) 035101.
[37] M. Ferer, G.S. Bromhal, D.H. Smith, Physica A 311 (2002) 5–22.
[38] J.P. Owejan, T.A. Trabold, D.L. Jacobson, D.R. Baker, D.S. Hussey, M. Arif, Int. J. Heat Mass Transfer 49 (2006) 4721–4731.
[39] C.-Y. Wang, Chem. Rev. 104 (2004) 4727–4766.
[40] J. Ge, H. Liu, J. Power Sources 160 (2006) 413–421.
[41] X.D. Xue, K.W.E. Cheng, D. Sutanto, Electrochim. Acta 52 (2006) 1135–1144.
[42] E. Birgersson, J. Nordlund, M. Vynnycky, C. Picard, G. Lindbergh, J. Electrochem. Soc. 151 (2004) A2157–A2172.
[43] U. Pasaogullari, C.-Y. Wang, J. Electrochem. Soc. 151 (2004) A399–A406.
[44] G. Lin, W. He, T. Van Nguyen, J. Electrochem. Soc. 151 (2004) A1999–A2006.
[45] R.G. Larson, L.E. Scriven, H.T. Davis, Nature 268 (1977) 409–413.
[46] M. Cieplak, M.O. Robbins, Phys. Rev. B 41 (1990) 11508–11521.
[47] V.P. Schulz, J. Becker, A. Wiegmann, P.P. Mukherjee, C.-Y. Wang, J. Electrochem. Soc. 154 (2007) B419–B426.
[48] J.T. Gostick, J. Power Sources (2007) doi: 10.1016/j.powsour.2007.04.059.